npj | Quantum Materials

www.nature.com/npjquantmats

ARTICLE OPEN

Correlation-driven electron-hole asymmetry in graphene field effect devices

Nicholas Dale[1,2], Ryo Mori[1,3], M. Iqbal Bakti Utama[2,3,4], Jonathan D. Denlinger[5], Conrad Stansbury[1,2], Claudia G. Fatuzzo[1,2,9], Sihan Zhao[1], Kyunghoon Lee[1,2], Takashi Taniguchi[6], Kenji Watanabe[7], Chris Jozwiak[5], Aaron Bostwick[5], Eli Rotenberg[5], Roland J. Koch[5], Feng Wang[1,2,8] and Alessandra Lanzara[1,2,8]✉

Electron-hole asymmetry is a fundamental property in solids that can determine the nature of quantum phase transitions and the regime of operation for devices. The observation of electron-hole asymmetry in graphene and recently in twisted graphene and moiré heterostructures has spurred interest into whether it stems from single-particle effects or from correlations, which are core to the emergence of intriguing phases in moiré systems. Here, we report an effective way to access electron-hole asymmetry in 2D materials by directly measuring the quasiparticle self-energy in graphene/Boron Nitride field-effect devices. As the chemical potential moves from the hole to the electron-doped side, we see an increased strength of electronic correlations manifested by an increase in the band velocity and inverse quasiparticle lifetime. These results suggest that electronic correlations intrinsically drive the electron-hole asymmetry in graphene and by leveraging this asymmetry can provide alternative avenues to generate exotic phases in twisted moiré heterostructures.

npj Quantum Materials (2022)7:9 ; https://doi.org/10.1038/s41535-021-00404-8

INTRODUCTION

Electron-hole asymmetry, or the difference in a material's electronic properties upon doping with electrons versus holes, profoundly impacts the character of phase transitions[1–5], and the choice of doping for devices[6,7]. While it typically arises from differing structures of bands containing electrons and holes[8,9], in some cases this asymmetry manifests from external sources such as impurities[10,11], strain[9,12,13], or simply from intrinsic many-body interactions[14–16]. Graphene is an interesting case in this light because its K point band structure is expected to be perfectly electron-hole symmetric[17], but the combination of its dimensionality and dispersion relation renders it highly susceptible to symmetry-breaking perturbations[18]. Most experimental realizations of the monolayer[16,19] and bilayer[20,21] exhibit electron-hole asymmetry, even after vast improvements in sample preparation, which reduce the effective strain and impurity concentration[16,21,22]. Whether external sources or intrinsic interactions, such as correlations[5,14–16,23,24] drive asymmetry remains to be verified. Understanding how electron-hole symmetry breaks and its relationship to exotic ground states[5,14,15,25] has become even more important with the recent discovery of Mott-like physics and superconductivity in twisted bilayer graphene[26,27] and other moiré heterostructures[28–30]. These systems exhibit phase diagrams reminiscent of the cuprates[31], in which the role of the strong electron-hole asymmetry in driving the remarkable phases remains elusive.

The difficulty in addressing the origin of electron-hole asymmetry in graphene today is the requirement of a probe that has complete access to the material self-energy in both energy and momentum spanning over a large range of electron and hole dopings. Some probes, including transport[19] and quantum capacitance[16], can easily cover the broad doping range via electrostatic gating, but are only sensitive to the electronic states at the Fermi energy (E_F) and do not provide any momentum information. In contrast, Angle-Resolved Photoemission Spectroscopy (ARPES) can provide access to the full quasiparticle spectral function $A(k, \omega)$, but so far has resorted to methods of doping that modify the fundamental properties of the system, including screening[32,33] and impurity concentration[34,35]. The very recent introduction of electrostatic gating into ARPES experiments[36,37] enables studies of the doping-dependent self-energy with full energy and momentum resolution while leaving the sample in pristine condition. Here, we directly reveal a significant electron-hole asymmetry in the quasiparticle self-energy of graphene. The doping and momentum resolution of our measurement enables us to provide strong evidence for correlations as the intrinsic driving force.

RESULTS

ARPES *in-operando*

Figure 1 a presents an illustration of the sample geometry used for the ARPES experiment and gating configuration, while panel b shows the optical micrograph of the overall sample S1 (two samples were measured in this report, see Methods section for details). The dashed contours identify regions of monolayer graphene (black), hBN (blue), and graphite (purple) while the yellow thick lines indicate the electrical contacts. The size of the sample is smaller than 1200 μm^2. The adopted beam size was 1 μm to allow measurements of each individual part of the sample

[1]Department of Physics, University of California, Berkeley, CA 94720, USA. [2]Materials Sciences Division, Lawrence Berkeley National Laboratory, Berkeley, CA 94720, USA. [3]Graduate Group in Applied Science & Technology, University of California, Berkeley, CA 94720, USA. [4]Department of Materials Science and Engineering, University of California at Berkeley, Berkeley, CA, USA. [5]Advanced Light Source, Lawrence Berkeley National Laboratory, Berkeley, CA 94720, USA. [6]International Center for Materials Nanoarchitectonics, National Institute for Materials Science, 1-1 Namiki, Tsukuba 305-0044, Japan. [7]Research Center for Functional Materials, National Institute for Materials Science, 1-1 Namiki, Tsukuba 305-0044, Japan. [8]Kavli Energy NanoSciences Institute at University of California Berkeley and Lawrence Berkeley National Laboratory, Berkeley, CA, USA. [9]Present address: Istituto di Scienze del Patrimonio Culturale, Consiglio Nazionale delle Ricerche (ISPC-CNR), Via Biblioteca 4, 95124 Catania, Italy. ✉email: Alanzara@lbl.gov

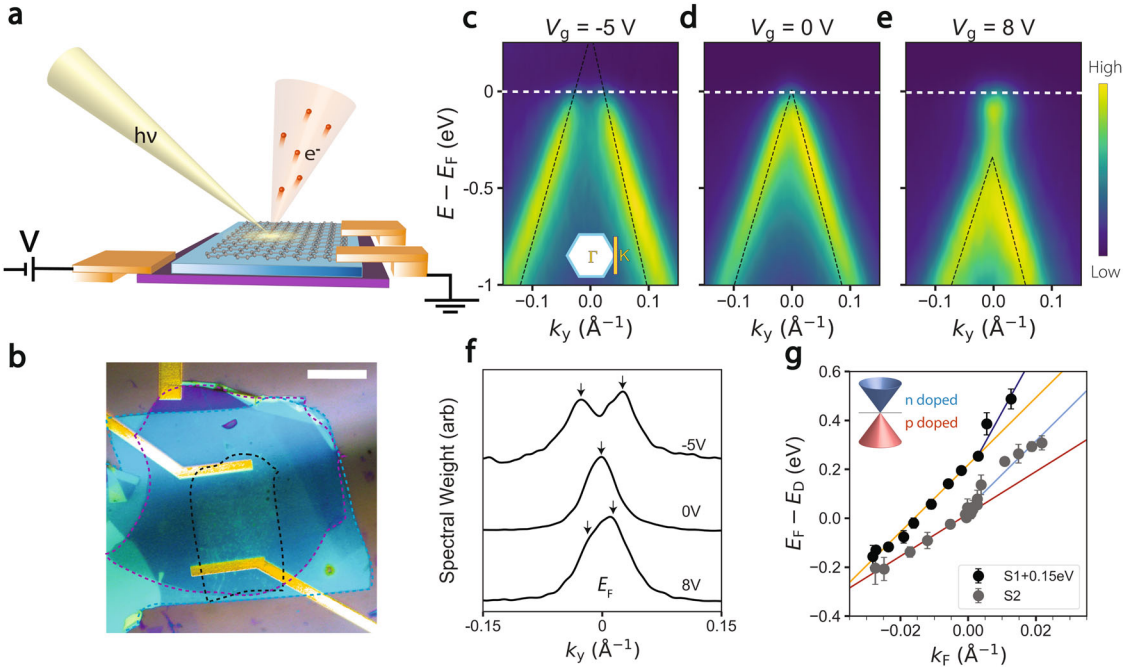

Fig. 1 ARPES *in-operando*. a, b. Schematic of experimental setup (**a-**) and optical micrograph of the graphene/hBN sample (**b-**). Dashed lines outline regions of graphene (black), hBN (blue), and graphite (purple). Scale bar: 20 μm (**c.-e.**) ARPES spectra for S1 along the $K - K'$ direction (perpendicular $\Gamma - K$) at (**c-**) p doping (-5V), (**d-**) equilibrium (0V), and (**e-**) n doping (8V). Blue dashed lines indicate quasiparticle peak positions extracted from Lorentzian fits. (**f.**) doping-dependent MDCs spectra and quasiparticle peak positions (black arrows) at E_F, indicated by the white dashed line in (b-d). (**g.**) $E_F - E_D$ as a function of k_F, extracted from linear fits to the graphene spectra. Data for two different samples are shown (S1 and S2). Error bars indicate 1σ deviation of best fit to the linear intersection of the dispersions. Orange (Red) line is a linear fit to the hole-doped E_F data for S1 (S2), Navy (Light blue) line is a fit to the electron-doped E_F data for S1 (S2).

and disentangle different contributions. The equilibrium spectra for the sample in Fig. 1d clearly depicts the characteristic linear bands of graphene's Dirac fermions along the K-K′ direction populated up to near the charge neutrality point. A positive (negative) voltage established between the graphite back gate and the graphene sample results in the addition, panel e (subtraction, panel c) of electrons to (from) the sample. Since the Fermi energy E_F is held at the ground, the additional negative (positive) charges shift the Dirac spectrum downward (upward). The doping change can be estimated by the peak separation at E_F from momentum distribution curves (MDCs), spectra at constant energy as a function of momentum, shown in panel f for different gating values. At $V_g = 0V$ the Fermi surface is a point and the momentum separation between MDC peaks is negligibly small. As electrons (holes) are added to the system, two peaks emerge and the momentum separation increases, with a maximum at $V_g = -5V(8V)$ corresponding to a p (n) doping of $2.2 \pm 0.3 \cdot 10^{12}\text{cm}^{-2}$ ($0.5 \pm 0.3 \cdot 10^{12}\text{cm}^{-2}$) (details on calculation of the carrier density can be found in Supplementary Note 1). The position of the Fermi energy $E_F - E_D$, displayed in Fig. 1g, is estimated by the intersection point of linear fits to the Dirac spectra (blue dashed lines in Fig. 1c–e). Assuming a linear dispersion relation, i.e., $E_F - E_D = v_F k_F$, the Fermi velocity v_F can be estimated here from a linear fit to the data in panel g. Interestingly, we find distinct behaviors on opposite sides of the charge neutrality point: at hole dopings, the estimated v_F (orange/red line) is less steep than v_F at neutrality and electron dopings (navy/blue lines). Although the results in Fig. 1g might appear in contrast to a previous report[38] where no asymmetry in the density of states was observed, we note that a true estimate of the density of states can only be reached by comparing E_F with quantities such as k_F that are unaffected by quantum capacitance contributions near charge neutrality (see Supplementary Note 5).

Electron-hole asymmetry in graphene dispersions

Figure 2 reports the detailed evolution of the K point electronic structure near E_F for different doping (gating) values. Figure 2a–c display raw image plots near the K point for dopings of $-0.9 \cdot 10^{12}\text{cm}^{-2}$, $0.0 \cdot 10^{12}\text{cm}^{-2}$, and $1.1 \cdot 10^{12}\text{cm}^{-2}$. Already from the raw data one can see that the spectrum in Fig. 2a is linear, and at the neutrality point (Fig. 2b) the dispersion looks noticeably steeper near E_F ($= E_D$) than at higher binding energies, in agreement with previous reports[32,33]. The electron-doped spectrum (Fig. 2c) presents different structure for the valence band than does the spectrum at similar hole doping: the valence band near the Dirac point (black dashed line) is steeper than the valence band in Fig. 2a (red dashed line).

These differences are better visualized by plotting the energy dispersion vs momentum (Fig. 2d), extracted by fitting the momentum distribution curves with standard Lorentzian-like functions in the proximity of the Dirac point. A clear departure from linearity is observed in the data starting at the neutrality point, where the dispersion is steepest, and still observed in the electron-doped side. Band velocities can be directly extracted from these data, being proportional to the slope of the ARPES dispersions. Because the dispersions for hole dopings remain linear, the band velocity at the Dirac point v_D (which is above E_F at these dopings) can be approximated by the Fermi velocity v_F. In contrast, the dispersions at neutrality (purple) and electron dopings (blue) show a large deviation from linearity, with v_D nearly twice as large as velocities at $E_D - 0.5$ eV. These results clearly indicate the presence of a distinct electron-hole asymmetry in the electronic response and are summarized in panel e, where the band velocities at the Dirac point (v_D), extracted from the slope of ARPES dispersions, are plotted as a function of doping. Although a divergence of v_D is observed in the proximity of the charge neutrality point, as previously reported[35] for the

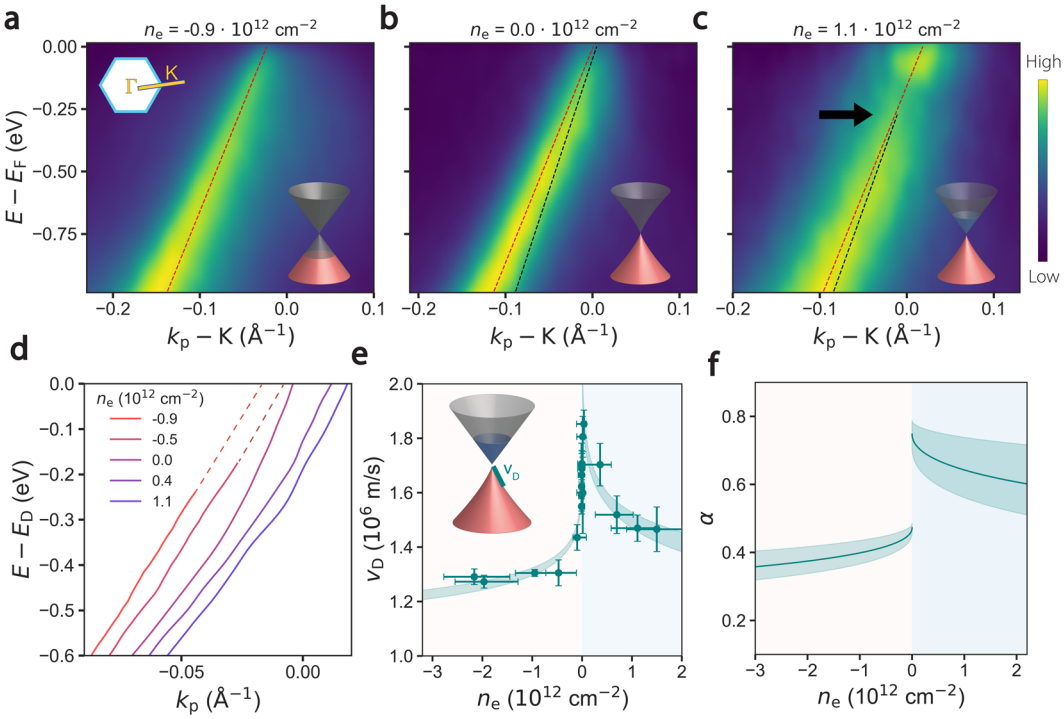

Fig. 2 Electron-hole asymmetry in graphene dispersions. (**a.-c.**) graphene spectra at three representative dopings: (**a.**) $-0.9 \cdot 10^{12}$cm^{-2}, (**b.**) $0.0 \cdot 10^{12}$cm^{-2}, (**c.**) $1.1 \cdot 10^{12}$cm^{-2}. Black (red) dashed lines indicate linear fits to dispersions near E_D (E_F in (**a**)). Inset cartoons illustrate the deviations from Dirac cone dispersions at respective dopings. (**d.**) E_D dispersions near the charge neutrality point indicate asymmetry in band velocity for electron and hole dopings. (**e.**) Extracted band velocities as a function of doping. Error bars indicate 1σ deviation of best fit to graphene dispersions. (**f.**) Graphene fine structure constant (α) as a function of doping, is extracted from band velocity fits. Teal shaded regions indicate 1σ deviation of best fit to the v_D data using the logarithm-based lineshape described in the text.

electron-doped side, a clear asymmetry is revealed over the entire doping range, with $v_D \sim 30\%$ higher for electron dopings than for hole dopings. The large renormalization of the Dirac spectra was previously reported at the neutrality point and assigned to electron-electron interactions[35,39] leading to a logarithmic correction of the band velocity via the coefficient α, which represents the long-range Coulomb coupling strength. Using a similar model[35]

$$\frac{v}{v_0} = 1 + \frac{\alpha}{8}\log\left(\frac{n_0}{n_e}\right) \quad (1)$$

we determine the coefficient $\alpha = e^2/\epsilon\hbar v_0$ (panel f), which is the primary contributor to the velocity enhancement. The dielectric strength $\epsilon = \epsilon_0(1 + a|n_e|^{1/2})$ is allowed to effectively increase as a function of doping[40,41] to account for charge-carrier screening in graphene[35], and $v_0 = 1.0 \cdot 10^6$ m/s is the local density approximation of the bare band velocity. The long-range coupling strength α shows a strong asymmetry between the electron and hole side, which is the driver for the asymmetry in the band dispersion discussed in panel d. We note that the correlation strength α is a direct measurement of charge-carrier screening and is independent from the substrate-induced screening, which could also modify v_D[42] but is doping independent[35]. Though this result is in apparent contrast with some reports using E_F sensitive probes[40,41], we note that the real Coulomb interaction strength α can be isolated more reliably from energy states at the Dirac point[35] rather than from states at E_F. Indeed, at E_F, the band velocity in graphene is modified by several interactions: notably it is enhanced by the long-range electron-electron interactions[33,35], and reduced by electron-phonon coupling[33,35,43,44]. In contrast, at the Dirac point the electron-phonon interaction becomes negligible due to the diminished density of states[45–47], and the band velocity is solely enhanced by the electron-electron interaction[39,48].

Electron-hole asymmetry in graphene imaginary self-energy

Figure 3 reports the imaginary part of the self-energy for holes and electrons at several doping values. The momentum distribution curve (MDC)'s FWHM Δk, the energy distribution curve (EDC)'s FWHM ΔE and the imaginary part of the self-energy Im $\Sigma(\omega)$ are related by $2\,\mathrm{Im}\,\Sigma(\omega) = \hbar v_F \Delta k = \Delta E$[49]. A clear asymmetry between electrons and holes is already apparent in the raw spectra, EDC (panel a) and MDC (panel b). The full doping dependence of Im Σ is plotted in Fig. 3c for both the MDCs at E_F (grey) and the EDCs at $E - E_D = -1.5$ eV (black), each showing a strong electron-hole asymmetry. Im Σ at E_F scales as $a_0\sqrt{|n_e|}$ away from neutrality, with the amplitude $a_0 = 0.30 \pm 0.05$ for electron dopings and $a_0 = 0.11 \pm 0.04$ for hole dopings. This doping dependence is in contrast to alkali-doped graphene samples, which develop a $1/\sqrt{n}$ dependence from the added long-range impurities[35], and the $\sqrt{n}$ scaling of the self-energy at E_F observed in gate-tunable graphene samples[50] can be attributed to the Matthiessen combination of acoustic and optical phonons[47,51,52] and short-range impurities[53,54]. The electron-electron interaction has been observed to modify the E_F self-energy contribution from phonons[43,44,47,55] and impurities[53,54,56] through a positive scaling with the renormalization parameter $\alpha = e^2/\epsilon\hbar v_F$ which denotes the strength of correlations. The asymmetry in α, as reported in Fig. 2, therefore drives the electron-hole asymmetry in the self-energy at E_F. We note that the choice of substrate is important to be able to discern the effect here described. Indeed, a competing electron-hole asymmetry such as the ones generated by moiré potential or breaking of inversion symmetry[13] as for example in the case of an aligned hBN substrate, might induce an overall reduction of the observed asymmetry.

Whereas techniques that are only sensitive to the low energy physics are often marred by impurities[19,34], the ability of ARPES to access the entire energy range allows us to extract the intrinsic

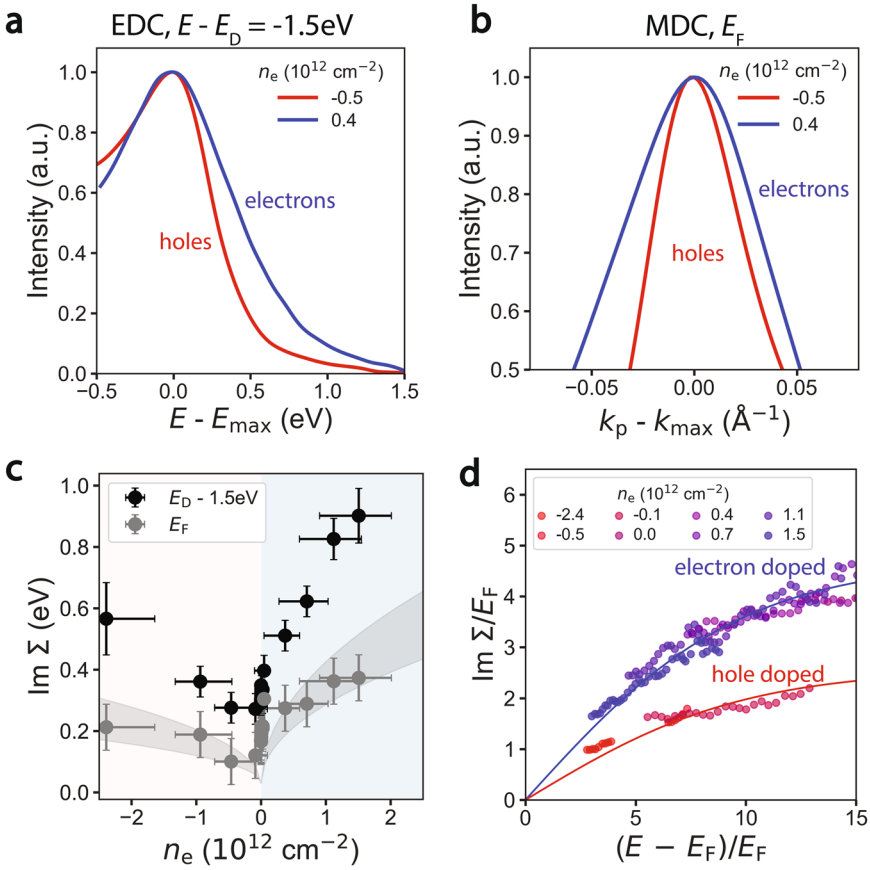

Fig. 3 Electron-hole asymmetry in graphene imaginary self-energy. (**a.**, **b.**) Normalized EDCs at $E - E_D = -1.5$ eV (**a-**), and MDCs at E_F (**b-**) for hole (red) and electron (blue) doped graphene. (**c.**) The imaginary part of the self-energy as a function of doping for EDCs at $E - E_D = -1.5$ eV (black) and MDCs at E_F (grey). Error bars indicate 1σ deviation obtained from peak fit to graphene spectral function. The shaded grey region indicates 1σ deviation of best fit to the square-root-based function described in the text. (**d.**) The imaginary part of the self-energy normalized by the Fermi energy. Blue (red) solid lines indicate fits to the data, as described in the text.

behavior of materials. Figure 3d presents the energy dependence of the imaginary self-energy scaled by the position of the Fermi energy E_F for different doping values. That $\mathrm{Im}\Sigma/E_F$ collapses to two distinct curves for electron and hole dopings provides further evidence for electron-hole asymmetry in the material. The reported energy dependence is qualitatively similar to numerical calculations of the inverse quasiparticle lifetime from dynamically screened electron-electron correlations[57,58]. From these calculations we can approximate the scattering rate to an empirical form:

$$\frac{\mathrm{Im}\Sigma_{ee}}{E_F} = c_1 \tanh\left[c_2 \cdot \frac{(E - E_F)}{E_F}\right] \quad (2)$$

where c_1 and c_2 are fit parameters. The fit shows an overall good agreement with the data and gives $c_{1h} = 2.5 \pm 0.2$ for hole dopings, $c_{1e} = 4.6 \pm 0.3$ for electron dopings, and $c_2 = 0.11 \pm 0.03$ for both dopings. Such differences are another manifestation of the electron correlation strength, as discussed in Ref. [58].

DISCUSSION

The data reported here provide evidence of a strong electron-hole asymmetry in graphene that is driven, as we will argue below, by strong electronic correlations. We now discuss the possible sources of such asymmetry and show that it is an intrinsic property rather than driven by disorder or other extrinsic effects.

As mentioned above, there are several mechanisms that break electron-hole symmetry in graphene, and include intrinsic asymmetries in the band structure, charged impurities, and electronic correlations. The asymmetries in the band structure are induced by the next-nearest-neighbor-hopping[17,59], which can be effectively enhanced by strain[12], induced for example from alignment to a substrate with a different lattice constant, and easily modeled by tight binding calculations[13]. When applying the latter to our experimental data, it becomes clear that to account for the 30% asymmetry between conduction and valence band velocity an unrealistic value of $|t'| \sim 3$ eV is needed. This is an order of magnitude larger than values reported in the literature ($t' \sim 0.3$ eV)[16,19,60] even when graphene is aligned to an hBN substrate[13], and opposite in sign to the asymmetry produced in graphene strained via wrinkles[12]. Moreover, we note that our samples are aligned at large twist angles to the hBN substrate, where lattice reconstruction is negligibly small[61] (see Supplementary Note 3 for more details), and therefore the effect on t' is negligible.

Another possible source of electron-hole asymmetry is the presence of charged impurities leading, in the case of very close (< 5 nm) proximity, to changes in the LDOS as large as 30%[12,22]. However, impurities produce an inverse quasiparticle lifetime that scales inversely with $E - E_D$[53], in contrast to the empirical function in equation 2 used to fit our data. Additionally, the impurity density required to produce this effect throughout a mesoscopic sample ($\sim 10^{13}$ cm^{-2}) is large enough to produce signatures in the spectral function in the form of resonance states[22,62,63] or impurity bands[64,65], which are not observed in our data.

These observations make electronic correlations the primary driver of electron-hole asymmetry observed in our study. Indeed, this interaction can consistently explain the asymmetric logarithmic renormalization of the dispersions across charge

neutrality[39,48], the nonlinear behavior of self-energy at high binding energies[57], and likely the asymmetry in the self-energy at E_F. Finally, we note that though numerical calculations for $\Sigma_{el\text{-}el}$[58] are much smaller than values found in our experiment, reaching quantitative agreement between experimental and theoretical results often requires additional scaling factors[45,66].

In conclusion, we have demonstrated the power of electrostatic gated ARPES to study the interplay of interactions and electron-hole symmetry in 2D materials. Our results point to electronic correlations as the driving force for an intrinsic electron-hole asymmetry in graphene, manifested in the dispersion and inverse quasiparticle lifetime. These findings open the intriguing possibility that electron-electron interactions might also be responsible for the asymmetries found in the phase diagrams of more strongly correlated materials, including twisted bilayer graphene[26,27], similar correlated 2D moiré systems[28,30,67], and in high-temperature cuprate superconductors[15,24,31,68]. Given that the moiré potential can be leveraged to enhance the strength of correlations in 2D heterostructures[30,69–71], we speculate that breaking electron-hole asymmetry via moiré-enhanced correlations can be an exciting alternative pathway to realize exotic quantum phases in twisted 2D heterostructures[5,14,15,25].

METHODS

Two devices were made for this experiment—for S1 refer to Fig. 1 and for S2 refer to Figs. 2 and 3

Sample preparation

Flakes of single-layer Graphene and hexagonal Boron Nitride were exfoliated onto Silicon Wafers with 90nm-thick oxide. S1 was constructed using a method similar to that used in[72]. A stamp comprised of Polypropylene carbonate (PPC), and Polydimethylsiloxane (PDMS), and the transparent tape was used to pick up Graphite, hBN, and Graphene in sequential order. The PPC stamp holding the stack was flipped onto a 90 nm oxidized Si wafer with the Graphene facing up, and the polymer was subsequently removed by annealing in a vacuum furnace at 350 C for 10 h. S2 was constructed using a technique similar to that outlined in Zomer et. al.[73]. A stamp comprised of Polycarbonate (PC) and Polydimethylsiloxane (PDMS) was used to pick up the Graphene, hBN, and Graphite to form a graphene/hBN/graphite heterostructure, which was then placed onto a fresh 90 nm-oxidized Si wafer. PC polymer residue was removed by placing the stack-on-chip in Chloroform for > 60 min at room temperature. Contacts were patterned onto each sample surface using electron-beam lithography followed by evaporation of 5 nm Cr and 50 nm Au.

ARPES measurements and analysis

Sample 1 was measured using a Scienta R4000 Hemispherical Analyzer at the nanoARPES branch of beamline 7.0.2 (MAESTRO) at the Advanced Light Source using a photon energy of 74 eV, a temperature of 300 K, and a pressure better than 1e-10 Torr. The beam was capillary refocused[74] to a spot size of ~1 μm × 1 μm. The overall energy and momentum resolution was 30 meV and 0.014 $\AA^{-1}$, respectively. The sample was doped electrostatically using a Keithley 2450 Source Meter.

Sample 2 was measured using a Scienta R8000 Hemispherical Analyzer at Beamline 4.0.3 (MERLIN)[75] at the Advanced Light Source using a photon energy of 94 eV, a temperature of 20 K, and a pressure better than 5e-11 Torr. The beamspot was ~100 μm × 50 μm. The overall energy and momentum resolution was 25 meV and 0.017 $\AA^{-1}$, respectively. The sample was doped electrostatically using a Keithley 2200 programmable power supply electrically connected to the cryostat.

All ARPES data in this paper were analyzed using pyARPES, an open-source python-based analysis framework[76]. Spectra presented in the figures have had a background (estimated by the mean value of detector counts $\simeq 0.5\AA^{-1}$ away from the K point) removed, and are smoothed by a gaussian filter with windows in momentum and energy smaller than the experimental resolution.

DATA AVAILABILITY

The data that support the findings of this study are available from the corresponding author upon reasonable request.

CODE AVAILABILITY

The analysis code used to support the findings of this study are available from the corresponding author upon reasonable request.

Received: 21 May 2021; Accepted: 28 November 2021;
Published online: 19 January 2022

REFERENCES

1. Sharpe, A. L. et al. Emergent ferromagnetism near three-quarters filling in twisted bilayer graphene. *Science* **365**, 605–608 (2019).
2. Sarkar, T. et al. Ferromagnetic order beyond the superconducting dome in a cuprate superconductor. *Science* **368**, 532–534 (2020).
3. Sajadi, E. et al. Gate-induced superconductivity in a monolayer topological insulator. *Science* **362**, 922–925 (2018).
4. Hsu, Y. T., Vaezi, A., Fischer, M. H. & Kim, E. A. Topological superconductivity in monolayer transition metal dichalcogenides. *Nat. Comm.* **8**, 14985 (2017).
5. Lee, S.-S., Ryu, S., Nayak, C. & Fisher, M. P. A. Particle-hole symmetry and the $\nu = 5/2$ quantum Hall state. *Phys. Rev. Lett.* **99**, 236807 (2007).
6. Arora, N. D., Hauser, J. R. & Roulston, D. J. Electron and hole mobilities in silicon as a function of concentration and temperature. *IEEE T. Electron Dev.* **29**, 292–295 (1982).
7. Larbalestier, D., Gurevich, A., Feldmann, D. M. & Polyanskii, A. High-T_c superconducting materials for electric power applications. *Nature* **414**, 368–377 (2001).
8. Ashcroft, N. & Mermin, D. *Solid State Physics* (Brooks/Cole Cengage Learning, Belmont, CA, 1976).
9. Jost, A. et al. Electron-hole asymmetry of the topological surface states in strained HgTe. *Proc. Natl. Acad. Sci. USA* **114**, 3381–3386 (2017).
10. Yazdani, A., Jones, B. A., Lutz, C. P., Crommie, M. F. & Eigler, D. M. Probing the local effects of magnetic impurities on superconductivity. *Science* **275**, 1767–1770 (1997).
11. Novikov, D. S. Numbers of donors and acceptors from transport measurements in graphene. *Appl. Phys. Lett.* **91**, 102102 (2007).
12. Bai, K.-K. et al. Detecting giant electron-hole asymmetry in a graphene monolayer generated by strain and charged-defect scattering via Landau level spectroscopy. *Phys. Rev. B* **92**, 121405(R) (2015).
13. DaSilva, A. M., Jung, J., Adam, S. & MacDonald, A. H. Transport and particle-hole asymmetry in graphene on boron nitride. *Phys. Rev. B* **91**, 245422 (2015).
14. Gross, D. J. & Neveu, A. Dynamical symmetry breaking in asymptotically free field theories. *Phys. Rev. D* **10**, 3235–3253 (1974).
15. Anderson, P. W. & Ong, N. P. Theory of asymmetric tunneling in the cuprate superconductors. *J. Phys. Chem. Solids* **67**, 1–5 (2006).
16. Kretinin, A. et al. Quantum capacitance measurements of electron-hole asymmetry and next-nearest-neighbor hopping in graphene. *Phys. Rev. B* **88**, 165427 (2013).
17. Neto, A. H. C., Guinea, F., Peres, N. M. R., Novoselov, K. S. & Geim, A. K. The electronic properties of graphene. *Rev. Mod. Phys.* **81**, 109–162 (2007).
18. Kotov, V. N., Uchoa, B., Pereira, V. M., Guinea, F. & Castro Neto, A. H. Electron-electron interactions in graphene: current status and perspectives. *Rev. Mod. Phys.* **84**, 1067–1125 (2012).
19. Deacon, R. S., Chuang, K.-C., Nicholas, R. J., Novoselov, K. S. & Geim, A. K. Cyclotron resonance study of the electron and hole velocity in graphene monolayers. *Phys. Rev. B* **76**, 081406(R) (2007).
20. Zou, K., Hong, X. & Zhu, J. Effective mass of electrons and holes in bilayer graphene: electron-hole asymmetry and electron-electron interaction. *Phys. Rev. B* **84**, 085408 (2011).
21. Zibrov, A. A. et al. Tunable interacting composite fermion phases in a half-filled bilayer-graphene Landau level. *Nature* **549**, 360–364 (2017).
22. Wang, Y. et al. Observing atomic collapse resonances in artificial nuclei on graphene. *Science* **340**, 734–737 (2013).
23. Novelli, P., Torre, I., Koppens, F. H. L., Taddei, F. & Polini, M. Optical and plasmonic properties of twisted bilayer graphene: impact of interlayer tunneling asymmetry and ground-state charge inhomogeneity. *Phys. Rev. B* **102**, 125403 (2020).
24. Cai, P. et al. Visualizing the evolution from the Mott insulator to a charge-ordered insulator in lightly doped cuprates. *Nat. Phys.* **12**, 1047–1051 (2016).
25. Angeli, M. & MacDonald, A. H. Γ valley transition metal dichalcogenide moiré bands. *Proc. Natl. Acad. Sci. USA* **118**, 1–5 (2021).
26. Cao, Y. et al. Unconventional superconductivity in magic-angle graphene superlattices. *Nature* **556**, 43–50 (2018).

27. Lu, X. et al. Superconductors, orbital magnets, and correlated states in magic angle bilayer graphene. *Nature* **574**, 20–23 (2019).
28. Park, J. M., Cao, Y., Watanabe, K., Taniguchi, T. & Jarillo-Herrero, P. Tunable strongly coupled superconductivity in magic-angle twisted trilayer graphene. *Nature* **590**, 249–255 (2021).
29. Chen, G. et al. Signatures of gate-tunable superconductivity in trilayer graphene/boron nitride moir\'e superlattice. *Nature* **572**, 215–219 (2019).
30. Wang, L. et al. Correlated electronic phases in twisted bilayer transition metal dichalcogenides. *Nat. Mater.* **19**, 861–866 (2020).
31. Gooding, R. J., Vos, K. J. E. & Leung, P. W. Theory of electron-hole asymmetry in doped CuO_2 planes. *Phys. Rev. B* **50**, 12866 (1994).
32. Hwang, H. Y. et al. Emergent phenomena at oxide interfaces. *Nat. Mater.* **11**, 103–113 (2012).
33. Siegel, D. A. et al. Many-body interactions in quasi-freestanding graphene. *Proc. Nat. Acad. Sci. USA* **108**, 11365–11369 (2011).
34. Chen, J. H. et al. Charged-impurity scattering in graphene. *Nat. Phys.* **4**, 377–381 (2008).
35. Siegel, D. A., Regan, W., Fedorov, A. V., Zettl, A. & Lanzara, A. Charge-carrier screening in single-layer graphene. *Phys. Rev. Lett.* **110**, 146802 (2013).
36. Nguyen, P. V. et al. Visualizing electrostatic gating effects in two-dimensional heterostructures. *Nature* **572**, 220–223 (2019).
37. Joucken, F. et al. Visualizing the effect of an electrostatic gate with angle-resolved photoemission spectroscopy. *Nano Lett.* **19**, 2682–2687 (2019).
38. Zhang, Y. et al. Giant phonon-induced conductance in scanning tunnelling spectroscopy of gate-tunable graphene. *Nat. Phys.* **4**, 627–630 (2008).
39. González, J., Guinea, F. & Vozmediano, M. A. Non-Fermi liquid behavior of electrons in the half-filled honeycomb lattice (a renormalization group approach). *Nucl. Phys. B* **424**, 595–618 (1994).
40. Elias, D. C. et al. Dirac cones reshaped by interaction effects in suspended graphene. *Nat. Phys.* **7**, 701–704 (2011).
41. Yu, G. L. et al. Interaction phenomena in graphene seen through quantum capacitance. *Proc. Natl. Acad. Sci. USA* **110**, 3282–3286 (2013).
42. Hwang, C. et al. Fermi velocity engineering in graphene by substrate modification. *Sci. Rep. UK* **2**, 2–5 (2012).
43. Zhou, S. Y., Siegel, D. A., Fedorov, A. V. & Lanzara, A. Kohn anomaly and interplay of electron-electron and electron-phonon interactions in epitaxial graphene. *Phys. Rev. B* **78**, 193404 (2008).
44. Siegel, D. A., Hwang, C., Fedorov, A. V. & Lanzara, A. Electron-phonon coupling and intrinsic bandgap in highly-screened graphene. *New J. Phys.* **14**, 095006 (2012).
45. Calandra, M. & Mauri, F. Electron-phonon coupling and electron self-energy in electron-doped graphene: Calculation of angular-resolved photoemission spectra. *Phys. Rev. B* **76**, 205411 (2007).
46. Li, Q. & Das Sarma, S. Finite temperature inelastic mean free path and quasiparticle lifetime in graphene. *Phys. Rev. B* **87**, 085406 (2013).
47. Sohier, T. et al. Phonon-limited resistivity of graphene by first-principles calculations: Electron-phonon interactions, strain-induced gauge field, and Boltzmann equation. *Phys. Rev. B* **90**, 125414 (2014).
48. Das Sarma, S., Hwang, E. H. & Tse, W.-K. Many-body interaction effects in doped and undoped graphene: Fermi liquid versus non-Fermi liquid. *Phys. Rev. B* **75**, 121406 (2007).
49. Valla, T. et al. Evidence for quantum critical behavior in the optimally doped cuprate $Bi_2Sr_2CaCu_2O_{8+\delta}$. *Science* **285**, 2110–2113 (1999).
50. Muzzio, R. et al. Momentum-resolved view of highly tunable many-body effects in a graphene/hBN field-effect device. *Phys. Rev. B* **101**, 201409(R) (2020).
51. Hwang, E. H. & Das Sarma, S. Acoustic phonon scattering limited carrier mobility in two-dimensional extrinsic graphene. *Phys. Rev. B* **77**, 115449 (2008).
52. Kaasbjerg, K., Thygesen, K. S. & Jacobsen, K. W. Unraveling the acoustic electron-phonon interaction in graphene. *Phys. Rev. B* **85**, 165440 (2012).
53. Adam, S., Hwang, E. H., Galitski, V. M. & Das Sarma, S. A self-consistent theory for graphene transport. *Proc. Natl. Acad. Sci. USA* **104**, 18392–18397 (2007).
54. Hwang, E. H. & Das Sarma, S. Single-particle relaxation time versus transport scattering time in a two-dimensional graphene layer. *Phys. Rev. B* **77**, 195412 (2008).
55. Attaccalite, C., Wirtz, L., Lazzeri, M., Mauri, F. & Rubio, A. Doped graphene as tunable electron-phonon coupling material. *Nano Lett.* **10**, 1172–1176 (2010).
56. Newaz, A. K., Puzyrev, Y. S., Wang, B., Pantelides, S. T. & Bolotin, K. I. Probing charge scattering mechanisms in suspended graphene by varying its dielectric environment. *Nat. Commun.* **3**, 734 (2012).
57. Hwang, E. H., Adam, S. & Sarma, S. D. Carrier transport in two-dimensional graphene layers. *Phys. Rev. Lett.* **98**, 2–5 (2007).
58. Tse, W.-K., Hwang, E. H. & Das Sarma, S. Ballistic hot electron transport in graphene. *Appl. Phys. Lett.* **93**, 023128 (2008).
59. Reich, S., Maultzsch, J., Thomsen, C. & Ordejón, P. Tight-binding description of graphene. *Phys. Rev. B* **66**, 035412 (2002).
60. Bostwick, A. et al. Band structure and many body effects in graphene. *Eur. Phys. J.-Spec. Top.* **148**, 5–13 (2007).
61. Jung, J., Dasilva, A. M., Macdonald, A. H. & Adam, S. Origin of band gaps in graphene on hexagonal boron nitride. *Nat. Commun.* **6**, 6308 (2015).
62. Peres, N. M. R., Guinea, F. & Castro Neto, A. H. Electronic properties of disordered two-dimensional carbon. *Phys. Rev. B* **73**, 125411 (2006).
63. Skrypnyk, Y. V. & Loktev, V. M. Spectral function of graphene with short-range impurity centers. *Low Temp. Phys.* **34**, 818–825 (2008).
64. Avsar, A. et al. Spin-orbit proximity effect in graphene. *Nat. Commun.* **5**, 4875 (2014).
65. Hwang, J. et al. Emergence of kondo resonance in graphene intercalated with cerium. *Nano Lett.* **18**, 3661–3666 (2018).
66. Park, C.-H., Giustino, F., Cohen, M. L. & Louie, S. G. Velocity renormalization and carrier lifetime in graphene from the electron-phonon interaction. *Phys. Rev. Lett.* **99**, 086804 (2007).
67. Chen, S. et al. Electrically tunable correlated and topological states in twisted monolayer-bilayer graphene. *Nat. Phys.* **17**, 374–380 (2020).
68. Phillips, P. Mottness. *Ann. Phys. New York* **321**, 1634–1650 (2006).
69. Cao, Y. et al. Correlated insulator behaviour at half-filling in magic-angle graphene superlattices. *Nature* **556**, 80–84 (2018).
70. Kerelsky, A. et al. Maximized electron interactions at the magic angle in twisted bilayer graphene. *Nature* **572**, 95–100 (2019).
71. Xu, Y. et al. Correlated insulating states at fractional fillings of moiré superlattices. *Nature* **587**, 214–218 (2020).
72. Utama, M. I. B. et al. Visualization of the flat electronic band in twisted bilayer graphene near the magic angle twist. *Nat. Phys.* **17**, 184–188 (2019).
73. Zomer, P. J., Guimaraes, M. H., Brant, J. C., Tombros, N. & Van Wees, B. J. Fast pick up technique for high quality heterostructures of bilayer graphene and hexagonal boron nitride. *Appl. Phys. Lett.* **105**, 4886096 (2014).
74. Koch, R. J. et al. Nano focusing of soft x-rays by a new capillary mirror optic. *Synch. Rad. News* **31**, 50–52 (2018).
75. Reininger, R. et al. MERLIN - A meV resolution beamline at the ALS. *AIP Conf. Proc.* **879**, 509–512 (2007).
76. Stansbury, C. & Lanzara, A. PyARPES: An analysis framework for multimodal angle-resolved photoemission spectroscopies. *SoftwareX* **11**, 100472 (2020).

ACKNOWLEDGEMENTS

We thank Salman Kahn for technical assistance in the sample fabrication setup, and Antonio Castro-Neto for helpful discussions. This work was primarily supported by the U.S. Department of Energy, Office of Science, Office of Basic Energy Sciences, Materials Sciences and Engineering Division under Contract No. DEAC02- 05CH11231 (Ultrafast Materials Science Program KC2203). K.W. and T.T. acknowledge support from the Elemental Strategy Initiative conducted by the MEXT, Japan, Grant Number JPMXP0112101001, JSPS KAKENHI Grant Number JP20H00354 and the CREST (JPMJCR15F3), JST.

AUTHOR CONTRIBUTIONS

N.D. and A.L. initiated and directed the research project. T.T. and K.W. synthesized the hBN crystals. N.D., M.I.B.U., S.Z., and K.L. fabricated the graphene samples. N.D., R.M., J.D.D., C.G.F., and A.B. performed the ARPES measurements. N.D. analyzed the ARPES data using software designed by C.S., and inputs from A.L., N.D., and A.L. wrote the manuscript, with inputs from all of the authors.

COMPETING INTERESTS

The authors declare no competing interests.

ADDITIONAL INFORMATION

Supplementary information The online version contains supplementary material available at https://doi.org/10.1038/s41535-021-00404-8.

Correspondence and requests for materials should be addressed to Alessandra Lanzara.